University of Reading

Systematic validation of an automated thalamic parcellation technique using anatomical data at 3T

Article

Published Version

Creative Commons: Attribution 4.0 (CC-BY)

Open Access

Williams, B. ORCID: https://orcid.org/0000-0003-3844-3117, Roesch, E. ORCID: https://orcid.org/0000-0002-8913-4173 and Christakou, A. ORCID: https://orcid.org/0000-0002-4267-3436 (2022) Systematic validation of an automated thalamic parcellation technique using anatomical data at 3T. NeuroImage, 258. 119340. ISSN 1053-8119 doi: 10.1016/j.neuroimage.2022.119340 Available at https://centaur.reading.ac.uk/105555/

It is advisable to refer to the publisher's version if you intend to cite from the work. See Guidance on citing.
Published version at: https://www.sciencedirect.com/science/article/pii/S1053811922004591
To link to this article DOI: http://dx.doi.org/10.1016/j.neuroimage.2022.119340

Publisher: Elsevier

All outputs in CentAUR are protected by Intellectual Property Rights law, including copyright law. Copyright and IPR is retained by the creators or other copyright holders. Terms and conditions for use of this material are defined in the End User Agreement.

University of Reading

www.reading.ac.uk/centaur

CentAUR

Central Archive at the University of Reading

Reading's research outputs online

NeuroImage 258 (2022) 119340

Contents lists available at ScienceDirect

NeuroImage

journal homepage: www.elsevier.com/locate/neuroimage

Systematic validation of an automated thalamic parcellation technique using anatomical data at 3T.

Brendan Williams[a,b,*], Etienne Roesch[a,b], Anastasia Christakou[a,b]

[a] Centre for Integrative Neuroscience and Neurodynamics, University of Reading, Reading, Berkshire, RG6 6AL, UK
[b] School of Psychology and Clinical Language Sciences, University of Reading, Reading, Berkshire, RG6 7BE, UK

ARTICLE INFO

Keywords:
Thalamus
Thalamic nuclei
Segmentation
MRI
Human Connectome Project

ABSTRACT

The thalamus is a brain region formed from functionally distinct nuclei, which contribute in important ways to various cognitive processes. Yet, much of the human neuroscience literature treats the thalamus as one homogeneous region, and consequently the unique contribution of specific nuclei to behaviour remains underappreciated. This is likely due in part to the technical challenge of dissociating nuclei using conventional structural imaging approaches. Yet, multiple algorithms exist in the neuroimaging literature for the automated segmentation of thalamic nuclei. One recent approach developed by Iglesias and colleagues (2018) generates segmentations by applying a probabilistic atlas to subject-space anatomical images using the FreeSurfer software. Here, we systematically validate the efficacy of this segmentation approach in delineating thalamic nuclei using Human Connectome Project data. We provide several metrics quantifying the quality of segmentations relative to the Morel stereotaxic atlas, a widely accepted anatomical atlas based on cyto- and myeloarchitecture. The automated segmentation approach generated boundaries between the anterior, lateral, posterior, and medial divisions of the thalamus. Segmentation efficacy, as measured by metrics of dissimilarity (Average Hausdorff Distance) and overlap (DICE coefficient) within groups was mixed. Regions were better delineated in anterior, lateral and medial thalamus than the posterior thalamus, however all the volumes for all segmented nuclei were significantly different to the corresponding region of the Morel atlas. These mixed results suggest users should exercise care when using this approach to study the structural or functional relevance of a given thalamic nucleus.

1. Introduction

The study of how the brain contributes to cognitive processes in human neuroimaging research often focuses on studying the cerebrum, while subcortical processes – and in particular the role of the thalamus – are typically understudied. However, an increased appreciation for the contribution of the thalamus in cognition is emerging in the neuroscientific literature (Wolff & Vann, 2019), echoing historic lesion based work (e.g. Bogousslavsky et al., 1988; Cheek & Taveras, 1966; Partlow et al., 1992; Schmahmann (2003); Van der Werf et al., 2000, 2003), and more recent functional work (e.g. Liebermann et al., 2013; Monchi et al., 2001; Schepers et al., 2017; Yang et al., 2020) that details the influence of the thalamus on cognition, and challenges the notion that the thalamus acts simply as a sensory-motor relay. Nevertheless, part of the challenge in studying the activity of the thalamus is due to the small size of its nuclei, relative to the spatial resolution typical of even high-field (3 Tesla) functional magnetic resonance imaging (MRI). A related issue is the delineation of functional and anatomical subdivisions of the thalamus. The appearance of the thalamus is largely homogenous when imaged using standard T1-weighted and T2-weighted contrast, requiring a high level of anatomical knowledge for manual segmentation. To define boundaries between different nuclei more accurately, image contrast in the thalamus can be enhanced by using specially developed sequences such as cortex attenuated inversion recovery and white-matter-nulled magnetization prepared rapid gradient echo (WMn MP-RAGE), or by combining 3D GRE phase data with optimised MPRAGE images (Bender et al., 2017; Magnotta et al., 2000; Tourdias et al., 2014). However, without automated segmentation algorithms for these enhanced contrast sequences (such as THOMAS for WMn MPRAGE data, see Su et al, (2019)), specialist expertise in neuroanatomy and neuroradiology are still required to accurately identify thalamic nuclei. Furthermore, the efficacy of these pulse sequences for increasing image contrast are attenuated at high-field (3 Tesla), relative to ultra-high field (7+ Tesla) strength MRI (Saranathan et al., 2015).

* Corresponding author: Centre for Integrative Neuroscience and Neurodynamics, School of Psychology and Clinical Language Sciences, University of Reading, Reading, Berkshire, RG6 6AL
E-mail address: b.williams3@reading.ac.uk (B. Williams).

https://doi.org/10.1016/j.neuroimage.2022.119340.
Received 6 December 2021; Received in revised form 20 May 2022; Accepted 28 May 2022
Available online 29 May 2022.
1053-8119/© 2022 The Authors. Published by Elsevier Inc. This is an open access article under the CC BY license (http://creativecommons.org/licenses/by/4.0/)

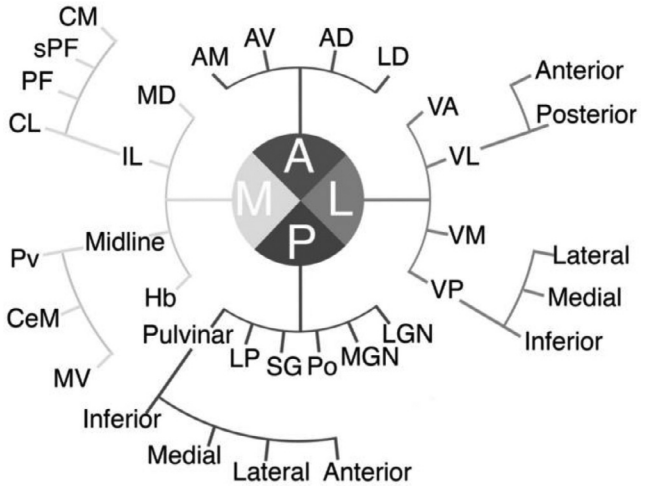

Figure 1. Hierarchical structure of thalamic nuclei as defined by the Morel stereotaxic atlas based on cytoarchitecture, myeloarchitecture, and functional relevance. Abbreviations: A – Anterior Group: AM – Anteromedial, AV – Anteroventral, AD – Anterodorsal, LD – Lateral Dorsal. L – Lateral Group: VA – Ventral Anterior, VM – Ventral Medial, VL – Ventral Lateral, VP – Ventral Posterior. P – Posterior Group: MGN – Medial geniculate nucleus, LGN – Lateral geniculate nucleus, Po – Posterior nucleus, SG – Suprageniculate/limitans, LP – Lateral Posterior. M – Medial Group: MD – Mediodorsal, CeM – Central Medial, Pv – Paraventricular, MV – Medioventral, Hb – Habenula, IL – Intralaminar, CL – Central Lateral, PF – Parafascicular, sPF – Subparafascicular, CM – Central Median. Figure reproduced from (Lambert et al., 2017) under a CC BY-NC-ND 4.0 license.

Recent studies have used MNI space parcellations (Krauth et al., 2010) to study the functional roles of thalamic nuclei. For instance, Geier et al., (2020) describe how the mediodorsal and anterior thalamic nuclei contribute in distinct ways to associative memory processes, while Huang et al, (2019) show how different cognitive demands produce dissociable modulatory responses in the mediodorsal nucleus and its functional connectivity with the prefrontal cortex, while also demonstrating that these dissociations are aberrant in schizophrenia. In both studies, MNI space thalamic parcellations created by Krauth et al, (2010) are derived from the Morel stereotaxic atlas (Morel, 2007; Morel et al., 1997). The Morel stereotaxic atlas is a widely used atlas of the thalamus derived from cytoarchitecture, myeloarchitecture, and functional relevance – using immunohistochemical staining of the calcium binding proteins parvalbumin, calbindin D-28k, and calretinin – to identify anatomical boundaries from five postmortem brain specimens (Figure 1). The Morel atlas thus provides a description of the anatomical structure of the thalamus that is not possible to acquire *in vivo* using magnetic resonance. Yet, the existence of this atlas in MNI space does not allow neuroscientists to infer subject-specific architecture, as it is based on the average of multiple individuals.

Numerous methods are described in the neuroimaging literature for defining the anatomical structure of thalamic nuclei using diffusion weighted, resting state, and anatomical data. Automated segmentation techniques first appear just after the turn of the century and include initial reports relying on anatomical (Amini et al., 2004; Deoni et al., 2007), diffusion data (Behrens et al., 2003; Johansen-Berg et al., 2005; Wiegell et al., 2003), and resting state functional data (Kim et al., 2013; Zhang et al., 2008). Parcellation methods have used prior knowledge of distinct cortico-thalamic connectivity to estimate structural boundaries within the thalamus using tractography (Behrens et al., 2003; Johansen-Berg et al., 2005), functional connectivity (Zhang et al., 2008), and machine learning approaches such as clustering algorithms (Amini et al., 2004; Deoni et al., 2007; Wiegell et al., 2003) or independent component analysis (Kim et al., 2013; Kumar et al., 2017). More recent approaches using anatomical, diffusion, and resting state data have been reviewed by Iglehart et al. (2020).

A recent, and alternative approach for using anatomical data was developed by Iglesias et al. (2018), and uses FreeSurfer to provide automated segmentations of thalamic nuclei. This approach involves the application of a probabilistic atlas to the anatomical image in subject space, using Bayesian inference to refine predicted locations: In this modelling framework prior knowledge of brain anatomy is combined with the likelihood of a given voxel intensity conditioned on the probability assignment to a given label. This model is used to estimate labels, which are progressively refined until a stable segmentation is obtained. This probabilistic atlas is in the form of a tetrahedral mesh that can adapt to changes in subject-specific differences in anatomy. The mesh was formed from a combination of ex-vivo MR images, histological staining, blockface photography, and in-vivo MRI. This approach may be preferable relative to techniques using resting state and diffusion data because it is able to delineate more nuclei with the thalamus, and is easier to apply. Additionally, this approach does not require the acquisition of data using specialist sequences, such as WMn MP-RAGE, meaning it is applicable to a wide range of existing and future datasets.

Having good subject-specific parcellation techniques for thalamic nuclei is important for both clinical practice and empirical research. For instance, these techniques could be used to guide surgeons when implanting deep brain stimulation electrodes to treat Parkinson's disease (Whiting et al., 2018). These techniques can also be used by researchers who may be interested in the role of different thalamic nuclei in functional processes, or the role of anatomical differences in health, development, and disease. Nevertheless, the effectiveness of segmentation approaches must first be validated before inferences can be made based on their output. In their original publication, Iglesias et al. (2018) provide volumetric comparisons between six segmented nuclei and their corresponding regions in the Morel atlas for 66 participants, yet these volumes are not statistically compared to each other, nor is the spatial specificity of segmentations quantified. Here, we aim to systematically compare the segmentation approach described by Iglesias et al. (2018) with regions in the Morel atlas. We provide volumetric, overlap, and isometric comparisons between all segmented regions and portions of the Morel atlas. These insights will allow clinicians and researchers to make informed decisions about the applicability of this segmentation approach for identifying specific thalamic nuclei in individuals.

2. Methods

2.1. Data acquisition

Anatomical data were sourced from the publicly available dataset of the Human Connectome Project (HCP) 1200 Subjects Data Release under the HCP Open Access Data Use terms (https://www.humanconnectome.org/study/hcp-young-adult/document/1200-subjects-data-release; Van Essen et al., 2013). The following description of data acquisition and preprocessing steps from the HCP project follow reporting guidelines from Horien et al. (2021) on the use of secondary neuroimaging datasets.

HCP data were acquired using a custom Siemens 3T Connectome Skyra scanner with a 32 channel receiver head coil and custom body transmission coil. Data were acquired over four separate scanning sessions; each session was approximately one hour in length. The structural data were acquired during one of those sessions. Two T1 weighted anatomical images were acquired using a 3D magnetization-prepared rapid gradient-echo (MP-RAGE) sequence with GeneRalized Autocalibrating Partially Parallel Acquisitions (GRAPPA) (R = 2) [TR = 2400ms; TE = 2.14ms; TI = 1000ms; slices = 256; voxel volume = 0.7mm^3; slice thickness = 0.7mm; distance factor = 50%; slice oversampling = 0.0%; FOV = 224 × 224mm; matrix = 320 × 320; flip angle = 8°; phase encoding direction = A → P; interleaved acquisition; echo spacing = 7.6ms].

2.2. Probabilistic atlas generation

The probabilistic atlas of Iglesias et al. (2018) was generated using data from 6 older adults *post mortem* who had no history of disease affecting brain morphology, and *in vivo* data from 39 younger adults. *Post mortem* brains were fixed by perfusing tissue *in situ* with 4% paraformaldehyde in phosphate buffer (pH 7.4); brains were then extracted and stored in 4% paraformaldehyde until *ex vivo* MRI scanning. Whole brain *ex vivo* images were acquired using a spatial resolution of 0.25mm isotropic using a 3D multi-slab balanced steady-state free precession sequence (McNab et al., 2009; see Iglesias et al., 2018 for all acquisition parameters). Following *ex vivo* imaging, *post mortem* tissue for the left and right hemispheres were separately sectioned into blocks, and blocks containing thalamic tissue were immersed in cryoprotectant. Tissue was cryosectioned into 50μm thick slices using a sliding microtome and blockface photos were taken for each section. Every tenth slice was Nissl stained for histological analysis, with individual nuclei delineated following the approach of Jones (2012).

Blockface photos were co-registered to oneanother, segmented from the block holder and microtome, and stacked to form a 3D volume. The 3D stack of blockface photos were used as an intermediary for registering *ex vivo* MRI and histologial data. Nuclear segmentations identified using Nissl staining were transformed into MRI space and refined to account for gaps between blocks. The probablistic atlas, based on a tetrahedral mesh, was built following the approach described by Iglesias et al. (2015). The generated tetrahedral mesh is locally adaptive to the shape of the thalamus, with each vertex of the mesh having an associated vector of probabilities for thalamic nuclei. The topology and resolution of the mesh varies based on anatomy, with finer detail in less uniform regions.

Segmentation using the probabilistic atlas is posed as a Bayesian inference problem, and is modelled with the following assumptions 1. The atlas is spatially warped following a deformation model 2. The segmentation of each voxel is drawn independently, based on the categorical distribution of the deformed atlas at that location 3. each nucleus in the atlas has a set of Gaussian parameters describing the image intensity of its voxels, which are drawn independently for each voxel. To segment the thalamus using the atlas, point estimates for Gaussian parameters and the atlas deformation model are computed. Point estimates are then updated using a coordinate ascent strategy, where Gaussian parameters and the atlas deformation model are updated alternately while the other parameter is fixed. The Gaussian parameters are estimated with the Expectation Maximization algorithm, while the atlas deformation model is updated with a conjugate gradient algorithm. The deformation model is initialised by fitting the atlas to the automated segmentation of the whole thalamus generated by recon-all in FreeSurfer. The posterior probability of a segmentation is calculated by the Expectation Maximization algorithm.

2.3. Preprocessing

Data were preprocessed using the HCP minimal preprocessing pipelines (Glasser et al., 2013; Smith et al., 2013; Sotiropoulos et al., 2013). Firstly, T1w images were corrected for gradient distortions using a customised version of gradient_nonlin_unwarp in FreeSurfer, then each subject's two T1w scans were aligned using FSL FLIRT and averaged. The averaged T1w image was then registered to MNI space using a 12 DOF affine registration with FLIRT, and a subset of 6 DOF transforms were used to align the anterior commissure, the anterior commissure – posterior commissure line, and the inter-hemispheric plane, while preserving the size and shape of the brain in native space. The skull was removed by inverting linear (FLIRT) and non-linear (FNIRT) warps from anatomical to MNI space, applying the warp to the MNI space brain mask, and then applying the mask to the averaged T1w image. Finally, the image was corrected for readout distortion and biases in B_1 and B_1+ fields.

2.4. Participants

One hundred participants were pseudo-randomly selected for inclusion in analysis. First, participants were filtered on the HCP database to include only subjects with complete anatomical, diffusion, and resting state acquisitions. Then subject IDs were sorted in ascending order and shuffled in MATLAB (2017b) using the seed 03112020 (the date of shuffling). The first one hundred subject IDs were chosen from this list for inclusion in analysis (Supplementary material 1).

2.5. Analysis

Data were processed following the method previously described by Iglesias et al., 2018. Data processing was run using a Nipype pipeline integrating FSL (version 6.0.4) and FreeSurfer (version 7.1.1) on Ubuntu 18.04.2. Output files from Nipype nodes were used as analytic checkpoints to confirm each step in the analysis ran as expected. Anatomical T1 images were first processed and parcellated using recon-all in FreeSurfer; the output of recon-all was used to initialise the parcellation of thalamic nuclei for anatomical data using the algorithm described by Iglesias et al. (2018). The parcellated thalamus was converted from FreeSurfer space to native anatomical space and changed from mgz to Nifti file format using mri_label2vol and mri_convert in FreeSurfer, respectively. Volumetric calculations for nuclei from the Morel atlas, and for segmented nuclei in subject space were performed using fslstats in FSL.

2.6. Comparison to Morel thalamic atlas

Linear rigid and affine transformations and non-linear warps between native anatomical space and MNI space were generated using the Advanced Normalization Tools (ANTs) package (Version 2.3.5, Ecphorella) script antsRegistrationSyN.sh (Avants et al., 2008). The ANTs package was selected due to its superior performance in registering skull-stripped images compared to other algorithms (Ou et al., 2014). Linear transformations and non-linear warps were then used to convert subject-level parcellations into MNI space. Parcellations in MNI space were re-binarised using a threshold of > 0.5.

Group-level probabilistic atlases were created by calculating a mean probability map for each parcellation in MNI space (described previously by Najdenovska et al. (2018)). Group-level segmentations were then compared to the Morel probabilistic atlas, which was used as ground truth (Krauth et al., 2010). Parcellations of thalamic nuclei in subject space generated by FreeSurfer, group-level mean probability maps in MNI space, plus linear transformations and non-linear warps from subject space to MNI_T1_1mm_brain space are available publicly at https://doi.org/10.17864/1947.000339.

Each parcellation was compared separately to individual nuclei in the Morel atlas using the EvaluateSegmentation toolbox (Taha & Hanbury, 2015), a threshold of > 0.25 was set for specificity metrics that do not accept non-binary input. The following metrics from the EvaluateSegmentation toolbox were used to assess each parcellation approach.

The DICE coefficient was used as a measure of overlap between segmentations and ground truth; it is a widely used measure in imaging processing for assessing the overlap between segmentation approaches. The DICE coefficient is defined as:

$$DICE(S_x, S_y) = \frac{2\left|S_x \cap S_y\right|}{\left|S_x\right| + \left|S_y\right|}$$

Where $|S_x \cap S_y|$is the cardinality of the intersection between the segmentation and ground truth (this is equal to the number of true positives, or overlapping voxels), divided by the sum of the cardinality of the ground truth $|S_x|$ and the segmentation $|S_y|$ (equal to the sum of true positives, false positives, and false negatives). Because the DICE coefficient is a measure of overlap, it is expressed in terms of the relationship

between true positives, false positives, and false negatives, but not the number of true negatives. Efficacious segmentations would have high overlap with their reference space of interest, yet overlap is not sufficient for determining the suitability of a segmentation approach as it cannot account for isometry.

The Average Hausdorff Distance is used as a measure of dissimilarity and can account for differences in isometry. Distance based metrics are advantageous – relative to overlap metrics in situations where segmentations are small – because overlap-based metrics disproportionately penalise errors in smaller than larger segmentations (Taha & Hanbury, 2015) as is the case with thalamic nuclei. Importantly, the Average Hausdorff Distance is sensitive to the position of false positives in a segmentation relative to ground truth, and therefore is a useful metric when considering the boundary of a segmentation, accounting for isometry. In relation to image segmentation, the Hausdorff Distance can be defined as the minimum number of voxels between a point in segmentation X and a point in segmentation Y. Therefore, the Average Hausdorff Distance is the average minimum distance between all points in segmentation A and segmentation B in voxels. The Average Hausdorff Distance is defined as:

$$\text{Average Hausdorff Distance}(A, B) = \max\left(d(A, B), d(B, A)\right)$$

$$d(A, B) = \frac{1}{N}\sum_{a \in A} \min_{b \in B} a - b$$

Where $d(A, B)$ is the average minimum distance ($\min a - b$) from voxels in the ground truth (A) to the segmentation (B), and $d(B, A)$ is the average minimum distance ($\min a - b$) from voxels in the segmentation (B) to the ground truth (A). The Average Hausdorff Distance is then the maximum of either of these two average distance measures in voxels.

As part of the volumetric comparison in Table 2, and Figures 4 & 7 the following nuclei from the Morel atlas were combined to make them comparable with the segmentations: LGN = (LGNmc + LGNpc), VA = (VAmc + VApc), VLp = (VLpd + VLpv), VPL = (VPLa + VPLp) (see Table 1 for an overview of abbreviations).

3. Results

3.1. Segmentation overlap

DICE coefficients between the Morel atlas and the group-level segmentations of the left and right thalamus are summarised in Figure 2 and Figure 3, respectively. On the x-axis are the thalamic nuclei from the Morel atlas; the segmented regions are displayed along the y-axis. A list of abbreviations used to refer to nuclei in text and in Figures 2, 3, 5, and 6 is presented in Table 1; the dendrograms presented above and adjacent to each heatmap show the hierarchical structure of the thalamus as defined by (Morel et al., 1997) and the relative position of each nucleus within that hierarchy, as presented in Table 1. Cells where groups of nuclei are equivalent between the Morel atlas and the segmentation are bound by a box. Here, when interpreting DICE coefficients, we use the following terminology, DICE = 0 no agreement, 0 < DICE < 0.2 slight agreement, 0.2 ≤ DICE < 0.4 fair agreement, 0.4 ≤ DICE < 0.6 moderate agreement, 0.6 ≤ DICE < 0.8 substantial agreement, 0.8 ≤ DICE ≤ 1 almost perfect agreement; these values have been used previously by (Pajula et al., 2012) for comparing Nifti images, and are a widely used convention for interpretating DICE coefficients.

DICE coefficients were similar between the left and right thalamus (Wilcoxon Signed-Ranks Test, Z = 9536, p = 0.531). Figure 2 and Figure 3 show that for the anterior nuclei, the AV had higher overlap than the LD. Overlap for anterior, lateral, medial, and posterolateral divisions of the lateral thalamus generally showed moderate to substantial overlap with nuclei from the same subregion, and mostly only slight overlap between subregions. Posterior thalamic nuclei had overlap values that were generally higher between subregions of the posterior thalamus than for other nuclear groups and were the only set of nuclei to show greater than slight agreement with nuclei from other nuclear groups. Of the midline nuclei in the medial thalamus, only the CeM was segmented, showing fair and moderate overlap in left and right hemispheres, respectively. For the intralaminar nuclei (CL, CM, Pf) the CM and Pf had higher overlap than the CL, which showed overlap with anterior and posterior at the upper end of slight agreement. Subregions of the mediodorsal thalamus (MDm and MDl) showed slight to moderate overlap with corresponding regions in the Morel atlas, and fair overlap with the CL in the left hemisphere.

3.2. Segmentation volume

Although nuclei volumes in the segmentation and the atlas were correlated ($t(42) = 5.869$, $r = 0.671$, $p < 0.001$; Figure 4), one sample t-tests showed that the volumes were significantly different for all nuclei (Table 2). Most volumes were smaller in the segmentation, except LGN, MDm, PuA, PuI, VLa, and VPL which bilaterally were larger in the segmentation than the equivalent volumes in the Morel atlas.

Bilaterally, the Average Hausdorff Distance (measured in voxels) between segmentations and the Morel atlas was lower along the diagonal (part of the same nuclear subgroup), and larger for nuclei off the diagonal, particularly for nuclei that were part of different nuclear groups (Figure 5, Figure 6). The lowest Average Hausdorff Distance between each segmented nuclei and a nucleus from the Morel atlas are summarised in Table 3; the lowest Average Hausdorff Distance between each nuclei in the Morel atlas and a segmented nucleus are summarised in Table 4.

Lastly, we calculated the Spearman's correlation coefficient between the volume of nuclei in the Morel atlas and the Average Hausdorff Distance of the group-level segmentation to determine whether nucleus size affected dissimilarity and found they were significantly anticorrelated $t(42) = -2.396$, $r = -0.347$, $p = 0.021$ (Figure 7). This trend was also significant when we correlated Average Hausdorff Distance of the group-level segmentation with the average segmentation volume ($t(42) = -3.458$, $r = -0.471$, $p = 0.001$). Visually, this trend looked like it was driven by segmentations with volumes at the tail end of the plot. These nuclei may have had particularly small volumes because they were not properly segmented by the algorithm. Therefore, we performed an exploratory analysis to test what effect removing these values had on the relationship. To do this we removed the five smallest nuclei bilaterally (CL, LD, L-Sg, VAmc, VM) which all had volumes lower than $21mm^3$, and used this as a threshold to re-run the correlation between the Average Hausdorff Distance of the group-level segmentation and the average segmentation volume. Removing these values reduced the strength of the relationship, and meant the correlation was non-significant $t(32) = -1.602$, $r = -0.273$, $p = 0.119$.

4. Discussion

The thalamus is known to be important for a wide range of cognitive processes, yet delineating and studying the roles of specific nuclei in aspects of cognition is a non-trivial problem in human neuroimaging. Here, we systematically compare the segmentation approach developed by Iglesias et al. (2018) to the Morel atlas of the thalamus (Krauth et al., 2010; Morel et al., 1997) using data from the Human Connectome project. We use DICE coefficients to measure volume overlap, and the Average Hausdorff Distance to compare the dissimilarity and isometry of segmentations relative to nuclei in the Morel atlas. Firstly, we found mixed levels of overlap across anterior, lateral, posterior, and medial portions of the thalamus, and at the group level we found the volumes for all nuclei were significantly different to the defined regions within the Morel atlas. Nuclei had lower Average Hausdorff Distances within groups than across groups, showing segmentations clearly discriminated between anterior, lateral, medial, and posterior portions of the thalamus.

Table 1
Definitions of thalamic nuclei as in the Morel atlas. Nuclei are ordered into their relevant anatomical groups and sub-groups. Abbreviations used in text and in figures for segmented regions and volumes in Morel atlas are given.

Nucleus	Group	Sub-group	Morel abbreviation	Segmentation abbreviation
Anterodorsal	Anterior		AD	
Anteromedial			AM	
Anteroventral			AV	AV
Lateral dorsal			LD	LD
Ventral anterior, magnocellular division	Lateral	*Ventral*	VAmc	VA VAmc
Ventral anterior, parvocellular division		*anterior*	VApc	
Ventral lateral anterior		*Ventral*	VLa	VLa
Ventral lateral posterior, dorsal division		*lateral*	VLpd	VLp
Ventral lateral posterior, ventral division			VLpv	
Ventral medial			VM	VM
Ventral posterior inferior		*Ventroposterior*	VPI	
Ventral posterior lateral, anterior division		*complex*	VPLa	VPL
Ventral posterior lateral, posterior division			VPLp	
Ventral posterior medial			VPM	
Lateral geniculate, magnocellular division	Posterior	*Geniculate*	LGNmc	LGN
Lateral geniculate, parvocellular division			LGNpc	
Medial geniculate			MGN	MGN
Posterior		*Posterior*	Po	
Suprageniculate		*complex*	SG	L-Sg
Lateral posterior			LP	LP
Anterior pulvinar		*Pulvinar*	PuA	PuA
Inferior pulvinar			PuI	PuI
Lateral pulvinar			PuL	PuL
Medial pulvinar			PuM	PuM
Habenula	Medial		Hb	
Central medial		*Midline*	CeM	CeM
Medioventral			MV	
Paraventricular			Pv	
Central lateral		*Intralaminar*	CL	CL
Centromedian			CM	CM
Parafascicular			Pf	Pf
Subparafascicular			sPf	
Mediodorsal, magnocellular division		*Mediodorsal*	MDmc	MDm
Mediodorsal, parvocellular division			MDpc	MDl

We assessed whether there was a systematic effect of volume on the isometry of segmented nuclei relative to the atlas. We found a significant negative correlation between the volume of nuclei in the Morel atlas and the Average Hausdorff Distance of segmentations, and between the size of the segmented volume and its Average Hausdorff Distance; the latter correlation was no longer significant after the five smallest nuclei (all with a volume $< 21mm^3$) were removed from the analysis, suggesting this relationship was driven by an inability to segment these nuclei with smaller values, rather than changes in isometry across nuclei size. In particular, the segmentation of smaller nuclei for individual subjects may be particularly sensitive to participant-related motion artefacts. These include head motion and physiology-related processes such as pulse, respiration, and swallowing; these motion sources can disturb the homogeneity of the magnetic field and the spatial localisation of signal, creating artefacts in the data (Williams & Lindner, 2020). Motion is a major issue during data acquisition, and the most effective way to minimise its effects is to correct for motion during data acquisition. For instance, head motion can be corrected online using techniques such as prospective motion correction (Callaghan et al., 2015), while correction for physiological processes could involve time locking data acquisition with specific phases of the cardiac or respiratory cycles (Zaitsev et al., 2015). Implementing either of these motion correction methods could improve the segmentation efficacy of all nuclei, and particularly smaller nuclei, by improving signal to noise ratio in data.

The segmentation approach developed by Iglesias et al. (2018) showed substantial overlap as indexed using the DICE coefficient for one nucleus within each of the anterior, lateral, posterior and medial thalamus (AV, VA, PuM, and CM respectively). Conversely, slight overlap between segmentations and their corresponding region in the Morel atlas was seen for a single segmentation in the anterior thalamus (VAmc), and four regions in the posterior thalamus (LGN, MGN, L-Sg, and LP). We hypothesise that segmentation of nuclei within the posterior thalamus may present difficulties that are not present for the anterior, lateral, and medial thalamus for the following reason. Adjacent to the pulvinar and protruding from the exterior surface of posterior thalamus, the geniculate nuclei may be misidentified as non-thalamic by the recon-all segmentation in FreeSurfer due to poor contrast relative to surrounding white matter on T1-weighted images (Fujita et al., 2001). This whole thalamus segmentation from recon-all is then used as a spatial prior for thalamic parcellation. If this spatial prior were under specified as it did not include the full extent of the geniculate nuclei, then the algorithm could have difficulty when segmenting these regions. Indeed, we see comparable DICE coefficients, particularly for the LGN, between the segmented LGN region and the inferior and lateral pulvinar regions as defined by the Morel atlas. Therefore, this misspecification may have a knock-on effect on the segmentation of the posterior thalamus as a whole. The posterior region was also the only portion of the thalamus to show greater than slight overlap with nuclei in other regions of the thalamus; both the LP and PuA showed fair bilateral overlap with the LD in the anterior thalamus, and the CL in the medial thalamus. Therefore, this segmentation approach formed clear anatomical boundaries between the anterior, lateral, and medial thalamus, but not the posterior thalamus. Additionally, the delineation of nuclei within each sub-region of the anterior, lateral, and medial thalamus appeared to be more distinct than in the posterior thalamus, as indicated by an increased number of nuclei with only slight overlap and being the only group of nuclei showing greater than slight overlap with nuclei from other groups. Nevertheless, we recommend that investigators studying the thalamus verify the efficacy of this segmentation approach for regions of interest using data from their own hardware, in addition to the results presented here.

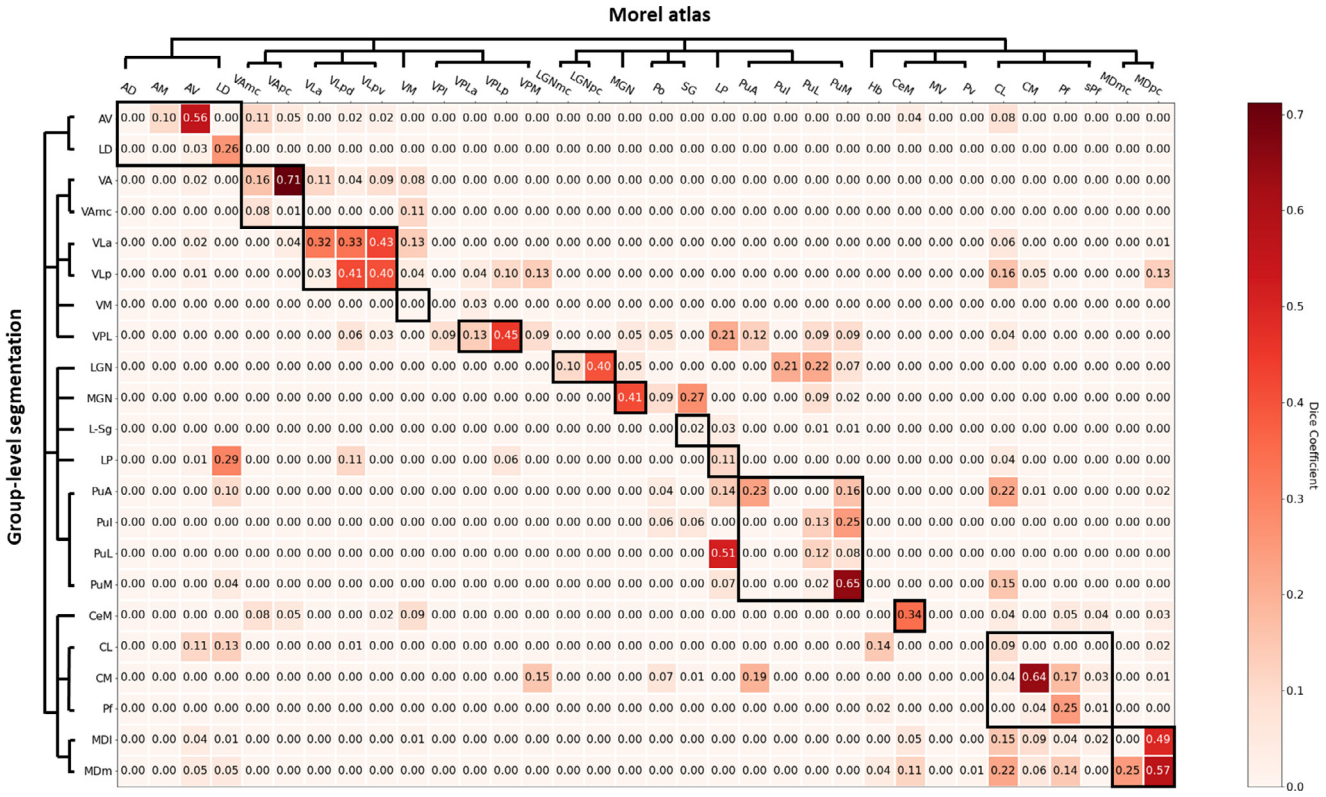

Figure 2. DICE coefficient between group-level segmented (vertical axis) regions and volumes in the Morel atlas (horizontal axis) in the left thalamus. Higher DICE coefficients show there is greater overlap between segmented regions and volumes in the Morel atlas. Dendrograms show the hierarchical structure of nuclei within the thalamus. DICE coefficients within BOLD boxes along the diagonal are regions that are part of the same nuclear group or sub-group; nuclei from the Morel atlas and segmented volumes are not always equivalent (see Table 1 for an overview of abbreviations).

There were significant volumetric differences for all nuclei between the volume as segmented by the automated algorithm and the Morel atlas. One potential explanation for this is that the Morel atlas, which was converted into MNI space (Krauth et al., 2010) was not corrected for the effects of fixation during the preparation of the tissue. Fixation with solutions such as formalin or paraformaldehyde is an important step when working with biological specimens as it limits the decomposition of biological tissue; yet fixation also causes tissue to shrink. The atlas derived by Morel from cyto- and myeloarchitecture was not corrected for shrinkage due to fixation (Bender et al., 2011), therefore, the atlas produced by Krauth et al, (2010) may include slight distortions of the morphometry of thalamic nuclei in-vivo. Another possible reason for our observed volumetric differences between the segmentation and the atlas is that the initial template used to begin segmentation is the whole thalamus volume estimated by *recon-all* in FreeSurfer. *Recon-all* has previously been shown to over-estimate the volume of the thalamus relative to manually derived segmentations of the whole thalamus, and in particular for participants with volumes at the lower end of the distribution (Makowski et al., 2018). Nevertheless, these explanations cannot fully describe why we observed volumetric differences for most nuclei as segmentations were generally smaller than those produced by the Morel atlas, with the exceptions being the LGN, MDm, PuA, PuI, and VLa. One reason may be that certain nuclei are overestimated and others are underestimated, while the general trend for nuclei volume remains consistent between segmentations and the Morel atlas. Our correlational results between segmented and atlas volumes suggest this may be the case, as we see a moderate positive correlation between the two sets of volumes. Improvements in volumetric estimation may be driven by combining diffusion and anatomical data as proposed by (Iglesias et al., 2019), yet there is currently no publicly available implementation for the approach they describe.

In their original paper describing their segmentation algorithm, Iglesias and colleagues do provide volumetric comparisons for six regions within the thalamus, namely the AV, LP, CM, MD (composite of MDl and MDm), VL (composite of VLa and VLp), and the pulvinar (PuA, PuM, PuL, and PuI combined) in 66 subjects. However, their approach involves the transformation of the equivalent Morel nuclei into subject space before plotting the distributions for each nucleus. Though this provides a visual overview of the relationship between segmented volumes and the Morel atlas, no inferential statistics are used to characterise this relationship. Additionally, though the authors state these regions were chosen based on their functional and structural connectivity, it is unclear why other nuclei were not also selected. Based on our metrics we see these regions appear well segmented at the group level, except for the LP. Here, we systematically show that, although there is a positive relationship between segmented volumes and volumes in the Morel atlas, these volumes are significantly different across all regions. Furthermore, we also extend upon the work of Iglesias et al. (2018) by describing differences in the overlap and isometry between segmented nuclei and regions within the Morel atlas and show that not all regions can be delineated as clearly as those selected in the original paper for comparison. These insights call for caution regarding the use of this segmentation approach to make inferences about the role these nuclei play in cognitive processes, or how aberrant changes in the thalamus occur in disease (Elvsåshagen et al., 2021; Park et al., 2020).

Accurate and reliable segmentation is especially important within the context of disease. Firstly, pathology may impair automated segmentations methods and increase variability relative to manual delineations in comparison to normative cases. At the volumetric level, automated FreeSurfer segmentations appear to delineate the whole thalamus at a level in-line with multiple manual human raters in cases of thalamic atrophy due to juvenile myoclonic epilepsy (Keller et al., 2012).

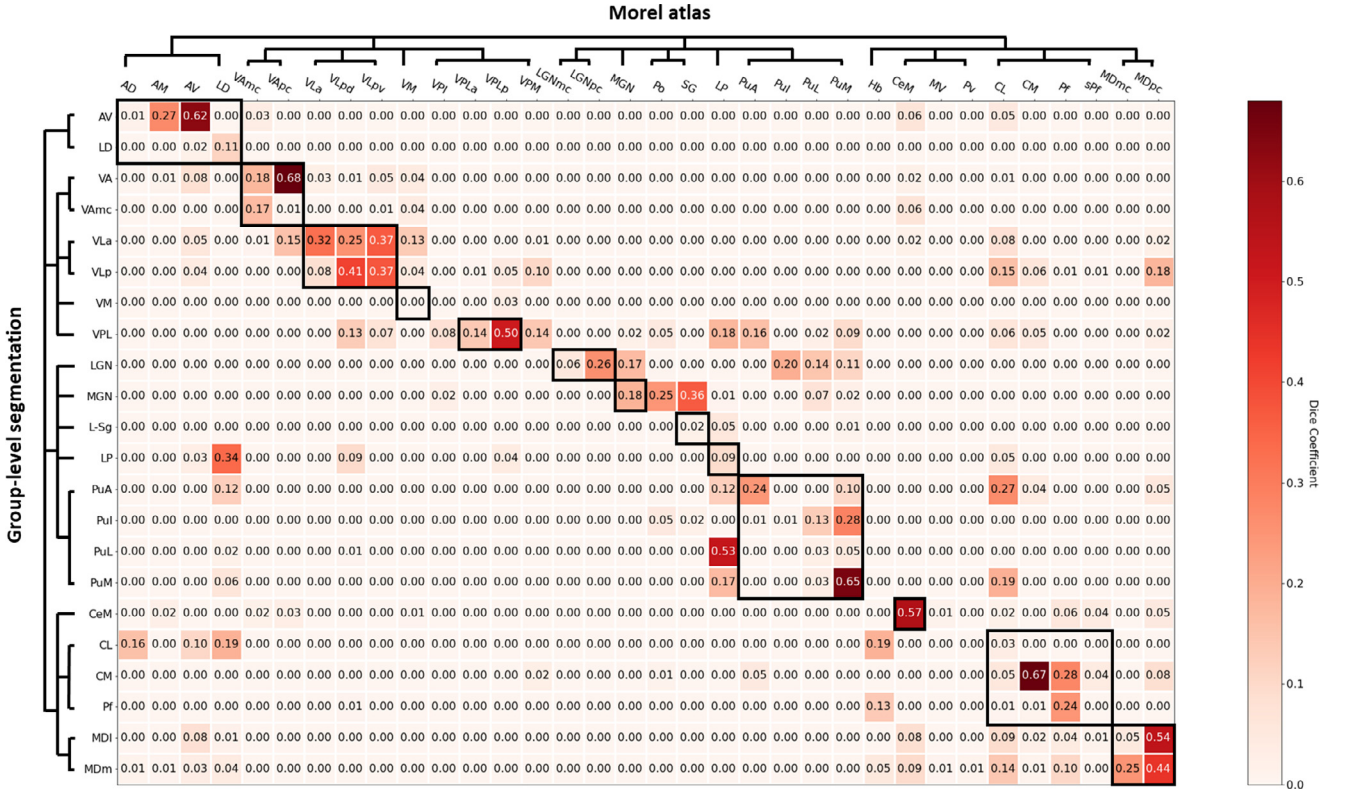

Figure 3. DICE coefficient between group-level segmented (vertical axis) regions and volumes in the Morel atlas (horizontal axis) in the right thalamus. Higher DICE coefficients show there is greater overlap between segmented regions and volumes in the Morel atlas. Dendrograms show the hierarchical structure of nuclei within the thalamus. DICE coefficients within BOLD boxes along the diagonal are regions that are part of the same nuclear group or sub-group; nuclei from the Morel atlas and segmented volumes are not always equivalent (see Table 1 for an overview of abbreviations).

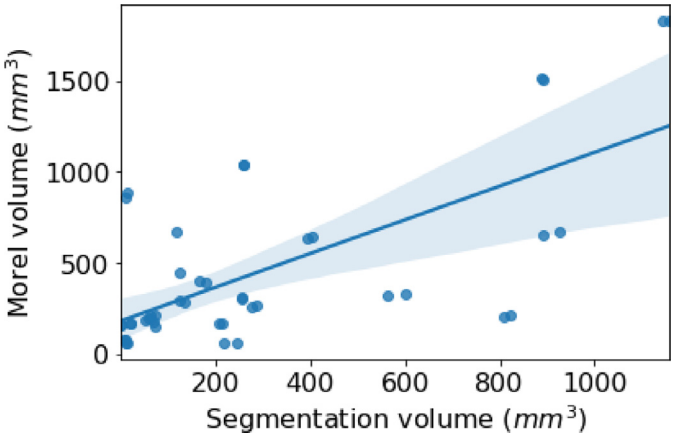

Figure 4. Spearman's correlation between group-level segmentation volumes and volumes from the Morel atlas. A significant moderate correlation was found between segmented volumes and volumes in the Morel atlas ($r = 0.671$, $p < 0.001$). The following regions within the Morel atlas are combined for the purpose of statistical analysis (LGN = (LGNmc + LGNpc), VA = (VAmc + VApc), VLp = (VLpd + VLpv), VPL = (VPLa + VPLp) (see Table 1 for an overview of abbreviations). The shaded region denotes 95% confidence intervals (bootstrapped, 1000 iterations).

However, automated segmentations of the whole thalamus appear to be less efficacious when compared with manual approaches. In multiple sclerosis, for instance, white matter lesion load is inversely correlated with the overlap between automated and manual thalamic delineations, and the difference in overlap between automated and manual thalamic delineations is significantly worse for multiple sclerosis cases than healthy controls (de Sitter et al., 2020). These effects are especially pertinent in multiple sclerosis when severe thalamic atrophy and cognitive impairment are observed (Burggraaff et al., 2021); in these cases, although FreeSurfer segmentations show good overlap with manual delineations, it is unclear how appropriate the spatial prior for the automated segmentation of individual thalamic nuclei would be. None of the participants used in the generation of the probabilistic atlas of Iglesias et al. (2018) had disorders that affected brain morphology, and therefore the atlas may sometimes deform innaccurately. This would then impact the identification of specific nuclei in space. Nevertheless, Iglesias et al. (2018) do demonstrate that the segmentation approach for individual thalamic nuclei can be used to classify individuals with Alzheimer's disease with greater accuracy than when the whole thalamus is used, suggesting there is some utility of this approach in cases of neurodegeneration.

Future developments to improve segmentation efficacy of Iglesias et al.'s (2018) tool could include the continued use of multimodal imaging for refining nuclear-level segmetations (Iglesias et al., 2019). As previously mentioned, the lateral geniculate nucleus is not well defined by standard T1-weighted contrast; however, proton densitiy imaging improves contrast between the lateral geniculate and surrounding white matter tissue (Fujita et al., 2001). Additionally, Proton density has been used for identifying the medial geniculate (Devlin et al., 2006) and centromedian (Kanowski et al., 2010) nuclei, while magnetisation transfer imaging also improves thalamic contrast (Gringel et al., 2009). Therefore, the inclusion of proton density images alongside T1-weighted and diffusion images could enhance the algorithm's performance, particularly within the posterior thalamus, since additional imaging contrasts could provide unique anatomical information. Furthermore, proton density and magnetisation transfer are advantageous for improving imaging contrast over other approaches

Table 2
Descriptive statistics for segmented thalamic volumes and regions within the Morel atlas. Mean, standard deviation and range are provided for each segmentation bilaterally. Additionally, the number of participants where this nuclei was delineated is specified. The following regions within the Morel atlas are combined for the purpose of statistical analysis (LGN = (LGNmc + LGNpc), VA = (VAmc + VApc), VLp = (VLpd + VLpv), VPL = (VPLa + VPLp) (see Table 1 for an overview of abbreviations).

Nucleus	Mean volume (mm^3)	Standard deviation	Minimum (mm^3)	Maximum (mm^3)	*t*-statistic	p-value	N	Morel volume (mm^3)
Left-AV	124.0254	18.205	84.035	174.93	-91.8059	1.3E-97	100	292
Left-CeM	72.74344	12.21982	49.735	109.417	-66.1624	9.34E-84	100	154
Left-CL	13.86406	9.645825	3.43	85.06399	-897.564	2.1E-195	100	884
Left-CM	255.2572	40.31033	173.558	417.431	-13.0186	3.57E-23	100	308
Left-LD	20.6143	8.264449	4.459	45.276	-172.627	1.4E-124	100	164
Left-LGN	285.1942	35.49029	199.969	382.445	6.502605	3.23E-09	100	262
Left-LP	123.0787	19.20904	89.18	180.075	-168.302	1.7E-123	100	448
Left-L-Sg	13.16777	9.164186	2.401	51.793	-49.7616	7.24E-72	100	59
Left-MDl	259.3183	26.47553	213.346	348.831	-291.512	4.6E-147	100	1035
Left-MDm	809.2776	79.1976	643.811	1083.88	75.66626	2.05E-89	100	207
Left-MGN	61.21521	17.20899	22.295	114.562	-87.7587	1.07E-95	100	213
Left-Pf	51.42599	12.4969	28.469	99.46999	-107.942	1.7E-104	100	187
Left-PuA	214.5877	24.80664	169.785	299.096	19.08727	5.98E-35	100	167
Left-PuI	246.9909	41.16957	170.814	355.691	45.43368	4.07E-68	100	59
Left-PuL	180.394	32.57992	125.881	320.019	-63.4027	5.76E-82	100	388
Left-PuM	1158.129	124.1217	906.892	1485.876	-54.019	2.85E-75	100	1832
Left-VA	394.7553	44.87643	293.951	497.693	-54.1532	2.25E-75	100	639
Left-VAmc	7.56658	2.362381	2.401	14.063	-279.804	2.6E-145	100	74
Left-VLa	561.9369	66.39361	411.943	770.0349	36.40699	3.95E-59	100	319
Left-VLp	891.0797	106.9382	662.3329	1262.24	-56.935	1.84E-77	100	1503
Left-VM	1.615819	1.311282	0.343	7.546	-1066.14	1.3E-171	83	156
Left-VPL	926.8751	123.0254	703.4929	1350.734	20.77518	7.15E-38	100	670
Right-AV	134.823	21.67799	82.32	182.476	-69.847	4.88E-86	100	287
Right-CeM	70.77805	11.77168	43.561	102.214	-86.4019	4.91E-95	100	173
Right-CL	11.92611	6.871285	3.087	61.74	-1222.25	1.1E-208	100	856
Right-CM	256.931	41.84041	184.534	423.262	-11.1933	2.79E-19	100	304
Right-LD	20.16154	7.981011	5.488	44.59	-179.322	3.2E-126	100	164
Right-LGN	275.8269	32.54821	202.37	360.493	5.449611	3.7E-07	100	258
Right-LP	117.0282	18.69873	74.088	163.611	-294.777	1.5E-147	100	671
Right-L-Sg	9.85782	6.783707	0.686	45.276	-70.6116	1.7E-86	100	58
Right-MDl	258.207	26.152	196.882	336.483	-295.541	1.2E-147	100	1035
Right-MDm	821.7388	79.12425	615.685	1072.561	77.0519	3.49E-90	100	209
Right-MGN	73.36427	19.29477	25.725	138.229	-71.4913	5.1E-87	100	212
Right-Pf	58.81078	13.84271	37.387	111.475	-96.4526	1E-99	100	193
Right-PuA	206.3351	23.58036	152.978	277.144	15.75376	1E-28	100	169
Right-PuI	219.0329	38.44851	140.973	320.705	40.63767	1.46E-63	100	62
Right-PuL	166.8009	31.07548	108.388	275.429	-73.7061	2.63E-88	100	397
Right-PuM	1145.116	119.2232	811.1949	1488.277	-57.408	8.29E-78	100	1833
Right-VA	403.9922	49.41994	299.096	566.9789	-48.5229	7.97E-71	100	645
Right-VAmc	9.02776	2.463819	4.459	15.778	-270.46	7.6E-144	100	76
Right-VLa	602.6201	77.34003	443.156	891.114	35.33016	6.25E-58	100	328
Right-VLp	887.7903	111.1463	639.6949	1288.651	-55.8796	1.11E-76	100	1512
Right-VM	1.437333	1.090426	0.343	5.145	-925.229	3.45E-90	42	159
Right-VPL	891.2992	118.3106	647.241	1254.008	19.78856	3.5E-36	100	656

such as WMn MP-RAGE (Tourdias et al., 2014), since sequences for Fast low angle shot MRI are readily available as a vendor product. While it is important to have segmentations that are faithful to their underlying neuroanatomy, it is also worth being pragmatic about the limitations of automated segmentations and how we use them. At the implementation level it is plausible that heterogeneity in segmentation efficacy will be observed across and within participants. This is despite Iglesias et al. (2018) demonstrating high test-retest reliability for most nuclei volumes. For example, these differences could be driven by changes in relative signal, intensity, and noise across multiple acquisitions within the same individual (Kiar et al., 2020). Other implementation-based sources of segmentation heterogeneity could include differences across operating systems and software versions. For example, estimates of segmentation volumes are inconsistent across versions of FreeSurfer (Gronenschild et al., 2012), and differences in floating point arithmetic across operating systems and FreeSurfer versions also influences analyses (Glatard et al., 2015). Practical solutions, such as the use of Docker and Singularity containers, enable the standardisation of computational resource, yet they cannot address inherent differences in image acquisition which could be alleviated by using multi-modal imaging contrasts.

More broadly, the biological plausibility of measures should also be considered when applying automated segmentation processes to study structure and function. Differences, such as those that are clinically relevant or that change across developmental trajectories, should be observed at a level that is greater than noise that could be due to within-individual variance or computational set-up. These differences, even if small, should be shown to be at least qualitatively reproducible. Additional considerations regarding biological plausibility include the application of automatic registration tools. As an example, the original pipeline in this study involved the use of FLIRT and FNIRT in FSL to convert images from subject space to MNI space. Yet, we found that these algorithms were unsuitable in terms of their accuracy for providing transformations within the thalamus. We therefore amended our pipeline to use ANTs, rather than FSL for normalisation. Additionally, it is worth considering the utility of applying these methods to studying functional changes using fMRI. For instance, the use of these segmentation techniques in studies with typical 3 tesla acquisition and analysis parameters ($3mm^3$ voxels, 8mm smoothing kernel) would mean that it is likely that functionally relevant signal is not localised to specific thalamic nuclei. Therefore, we suggest that those wishing to study the relevance of thalamic nuclei to functional processes carefully consider

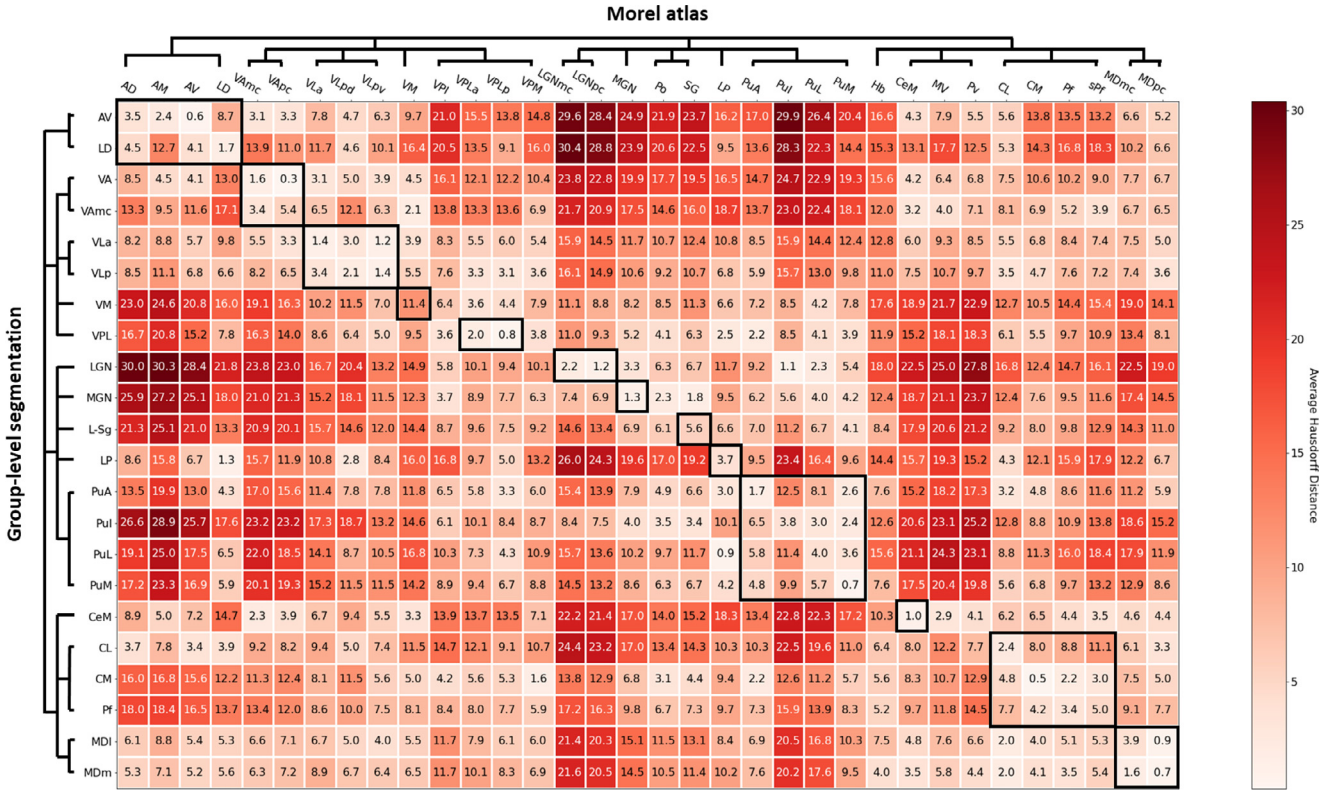

Figure 5. Average Hausdorff Distance between group-level segmented (vertical axis) regions and volumes in the Morel atlas (horizontal axis) in the left thalamus. Higher Average Hausdorff Distances shows there is greater dissimilarity and that segmented regions and volumes in the Morel atlas are less isometric. Dendrograms show the hierarchical structure of nuclei within the thalamus. Average Hausdorff Distances within BOLD boxes along the diagonal are show regions that are part of the same nuclear group or sub-group; nuclei from the Morel atlas and segmented volumes are not always equivalent (see Table 1 for an overview of abbreviations).

Table 3
Lowest Average Hausdorff Distance between each group-level segmentation and its corresponding volume within the Morel atlas. Higher Average Hausdorff Distances shows there is greater dissimilarity and that segmented regions and volumes in the Morel atlas are less isometric (see Table 1 for an overview of abbreviations).

Segmentation Left	Morel	Distance (voxels)	Segmentation Right	Morel	Distance (voxels)
VA	Vapc	0.332751	VA	VApc	0.431525
CM	CM	0.460216	CM	CM	0.437139
AV	AV	0.63198	AV	AV	0.515158
PuM	PuM	0.659518	CeM	CeM	0.542475
MDm	MDpc	0.735318	PuL	LP	0.66192
VPL	VPLp	0.782243	VPL	VPLp	0.663946
MDl	MDpc	0.873007	MDl	MDpc	0.709001
PuL	LP	0.878453	PuM	PuM	0.74441
CeM	CeM	1.00372	MDm	MDpc	1.047935
LGN	PuI	1.130774	LP	LD	1.163396
VLa	VLpv	1.19992	MGN	SG	1.354912
LP	LD	1.255153	VLa	VLa	1.363725
MGN	MGN	1.334352	VLp	VLpv	1.453629
VLp	VLpv	1.364389	LGN	PuI	1.493237
PuA	PuA	1.666463	PuI	PuM	1.843849
LD	LD	1.743449	VAmc	CeM	1.864043
VAmc	VM	2.13865	PuA	PuA	1.943745
PuI	PuM	2.371877	CL	AD	2.583181
CL	CL	2.379825	LD	LD	2.850019
Pf	Pf	3.431893	Pf	Pf	3.263468
VM	VPLa	3.63583	VM	VPLp	3.556207
L-Sg	PuM	4.061324	L-Sg	PuM	4.555451

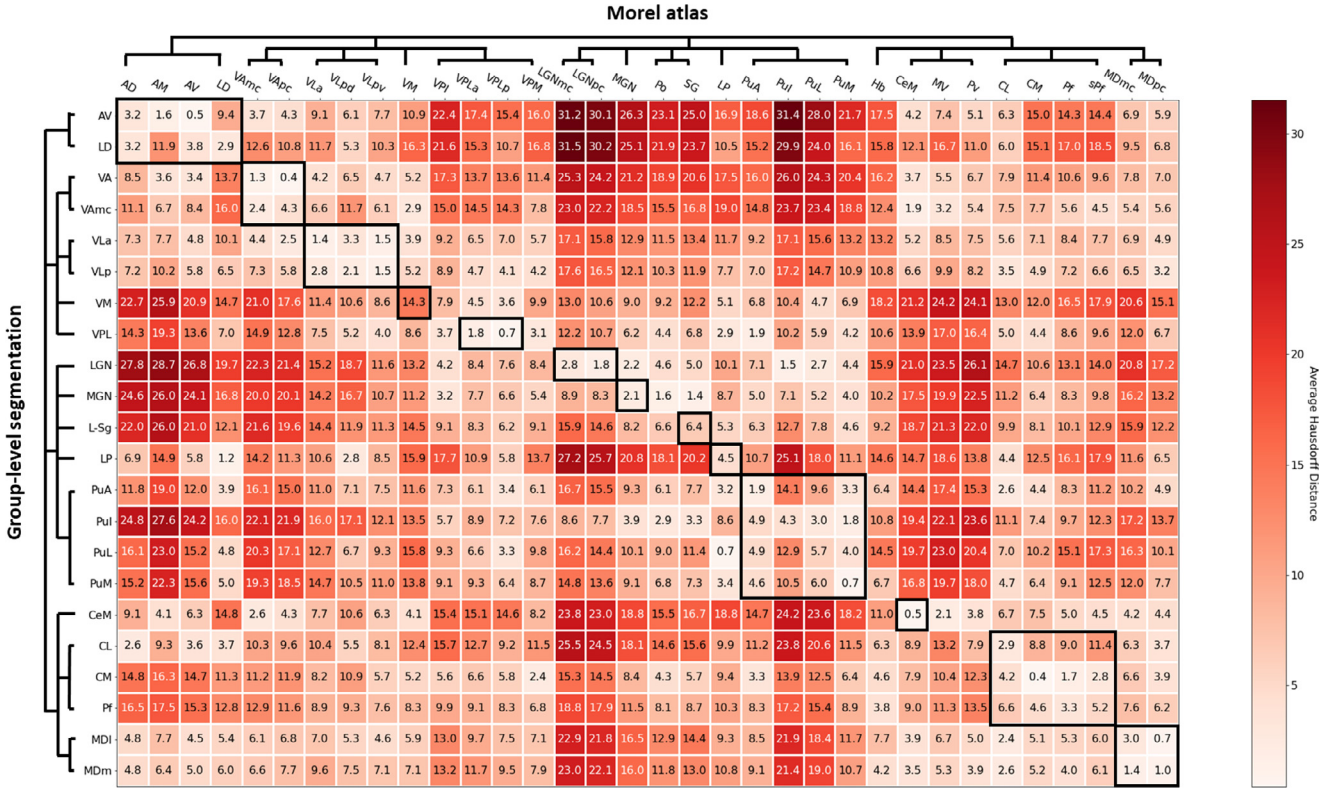

Figure 6. Average Hausdorff Distance between group-level segmented (vertical axis) regions and volumes in the Morel atlas (horizontal axis) in the right thalamus. Higher Average Hausdorff Distances shows there is greater dissimilarity and that segmented regions and volumes in the Morel atlas are less isometric. Dendrograms show the hierarchical structure of nuclei within the thalamus. Average Hausdorff Distances within BOLD boxes along the diagonal are show regions that are part of the same nuclear group or sub-group; nuclei from the Morel atlas and segmented volumes are not always equivalent (see Table 1 for an overview of abbreviations).

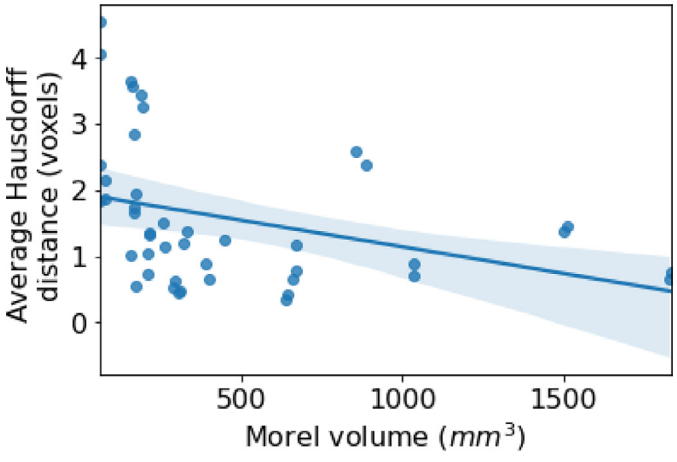

Figure 7. Spearman's correlation between the volume of nuclei in the Morel atlas and the Average Hausdorff Distance of the group-level segmentation. A significant weak correlation was found between segmented volumes and Average Hausdorff Distances (r = -0.347, p = 0.021). The following regions within the Morel atlas are combined for the purpose of statistical analysis (LGN = (LGNmc + LGNpc), VA = (VAmc + VApc), VLp = (VLpd + VLpv), VPL = (VPLa + VPLp) (see Table 1 for an overview of abbreviations). The shaded region denotes 95% confidence intervals (bootstrapped, 1000 iterations).

acquisition and processing pipelines with respect to the metrics provided here to restrict the integration of signal across regions of the thalamus. For instance, investigators may find it beneficial to combine segmentations from regions with high overlap and functional homogeneity, such as the subnuclei of the mediodorsal thalamus, to improve the anatomical definition of their region of interest. Furthermore, consideration of the size of segmented nuclei in relation to acquisition and processing parameters are important to determine whether it could be considered feasible to acquire clean signal from a given region.

In conclusion, this paper aimed to systematically validate the thalamic nuclei segmentation approach developed by Iglesias et al. (2018) using Human Connectome Project data and the Morel thalamic atlas derived from histological staining post-mortem (Krauth et al., 2010). Using volumetric, overlap, and isometry measures we show that the automated segmentation approach delineates between the anterior, lateral, posterior, and medial portions of the thalamus, and that there is mixed segmentation efficacy for individual nuclei within these groups. Importantly, we find that the volumes for segmented nuclei are significantly different from those defined in the Morel atlas, calling for caution when adopting this segmentation method. We also suggest important considerations related to the functional relevance of these segmentations, describe potential pitfalls researchers may face when using these segmentations within their own research, and recommend investigators undertake further validation work in addition to the results presented here when using this approach.

Parcellations of thalamic nuclei in subject space generated by FreeSurfer, group-level mean probability maps in MNI space, plus linear transformations and non-linear warps from subject space to MNI_T1_1mm_brain space are available publicly at https://doi.org/10.17864/1947.000339.

Funding

Brendan Williams was funded by the Magdalen Vernon PhD Studentship of the School of Psychology and Clinical Language Sciences,

Table 4
Lowest Average Hausdorff Distance between volumes within the Morel atlas and its corresponding group-level segmentation. Higher Average Hausdorff Distances shows there is greater dissimilarity and that segmented regions and volumes in the Morel atlas are less isometric (see Table 1 for an overview of abbreviations).

Morel Left	Segmentation	Distance (voxels)	Morel Right	Segmentation	Distance (voxels)
VApc	VA	0.332751	VApc	VA	0.431525
CM	CM	0.460216	CM	CM	0.437139
AV	AV	0.63198	AV	AV	0.515158
PuM	PuM	0.659518	CeM	CeM	0.542475
MDpc	MDm	0.735318	LP	PuL	0.66192
VPLp	VPL	0.782243	VPLp	VPL	0.663946
LP	PuL	0.878453	MDpc	MDl	0.709001
CeM	CeM	1.00372	PuM	PuM	0.74441
PuI	LGN	1.130774	LD	LP	1.163396
LGNpc	LGN	1.19418	VAmc	VA	1.270166
VLpv	VLa	1.19992	SG	MGN	1.354912
LD	LP	1.255153	VLa	VLa	1.363725
MGN	MGN	1.334352	MDmc	MDm	1.407938
VLa	VLa	1.379999	VLpv	VLp	1.453629
VAmc	VA	1.618183	PuI	LGN	1.493237
VPM	CM	1.636273	AM	AV	1.636578
MDmc	MDm	1.646026	Po	MGN	1.641001
PuA	PuA	1.666463	Pf	CM	1.693499
SG	MGN	1.757686	LGNpc	LGN	1.762076
CL	MDm	1.963445	VPLa	VPL	1.82221
VPLa	VPL	1.971193	PuA	VPL	1.909816
VLpd	VLp	2.128442	VLpd	VLp	2.062684
VM	VAmc	2.13865	MGN	MGN	2.08619
LGNmc	LGN	2.169776	MV	CeM	2.137629
Pf	CM	2.18454	VPM	CM	2.396707
Po	MGN	2.294516	CL	MDl	2.447928
PuL	LGN	2.330049	AD	CL	2.583181
AM	AV	2.39251	PuL	LGN	2.668344
MV	CeM	2.945644	sPf	CM	2.785892
sPf	CM	3.005708	LGNmc	LGN	2.818837
AD	AV	3.470230	VM	VAmc	2.924402
VPI	VPL	3.562672	VPI	MGN	3.220601
Hb	MDm	4.016412	Pv	CeM	3.809648
Pv	CeM	4.120213	Hb	Pf	3.843084

University of Reading. Funding for article processing charges was provided by the University of Reading.

Declaration of Competing Interest

None

Credit authorship contribution statement

Brendan Williams: Conceptualization, Methodology, Software, Formal analysis, Investigation, Resources, Data curation, Writing – original draft, Writing – review & editing, Visualization, Project administration, Funding acquisition. **Etienne Roesch:** Software, Resources, Writing – review & editing, Supervision. **Anastasia Christakou:** Conceptualization, Resources, Writing – review & editing, Supervision, Project administration, Funding acquisition.

Acknowledgements

The authors would like to thank ETH Zurich and the University of Zurich for the provision of the Morel atlas in MNI space as described in (Krauth et al., 2010). Data were provided by the Human Connectome Project, WU-Minn Consortium (Principal Investigators: David Van Essen and Kamil Ugurbil; 1U54MH091657) funded by the 16 NIH Institutes and Centers that support the NIH Blueprint for Neuroscience Research; and by the McDonnell Center for Systems Neuroscience at Washington University.

Supplementary materials

Supplementary material associated with this article can be found, in the online version, at doi:10.1016/j.neuroimage.2022.119340.

References

Amini, L., Soltanian-Zadeh, H., Lucas, C., Gity, M., 2004. Automatic segmentation of thalamus from brain MRI integrating fuzzy clustering and dynamic contours. IEEE Transactions on Biomedical Engineering 51 (5), 800–811. doi:10.1109/TBME.2004.826654.

Avants, B.B., Epstein, C.L., Grossman, M., Gee, J.C., 2008. Symmetric diffeomorphic image registration with cross-correlation: Evaluating automated labeling of elderly and neurodegenerative brain. Medical Image Analysis 12 (1), 26–41. doi:10.1016/j.media.2007.06.004.

Behrens, T.E.J., Johansen-Berg, H., Woolrich, M.W., Smith, S.M., Wheeler-Kingshott, C.A.M., Boulby, P.A., Barker, G.J., Sillery, E.L., Sheehan, K., Ciccarelli, O., Thompson, A.J., Brady, J.M., Matthews, P.M., 2003. Non-invasive mapping of connection between human thalamus and cortex using diffusion imaging. Nature Neuroscience 6 (7), 750–757. doi:10.1038/nn1075.

Bender, B., Mänz, C., Korn, A., Nägele, T., Klose, U., 2011. Optimized 3D Magnetization-Prepared Rapid Acquisition of Gradient Echo: Identification of Thalamus Substructures at 3T. American Journal of Neuroradiology 32 (11), 2110–2115. doi:10.3174/ajnr.A2705.

Bender, B., Wagner, S., Klose, U., 2017. Optimized depiction of thalamic substructures with a combination of T1-MPRAGE and phase: MPRAGE*. Clinical Neuroradiology 27 (4), 511–518. doi:10.1007/s00062-016-0513-4.

Bogousslavsky, J., Regli, F., Uske, A., 1988. Thalamic infarcts: clinical syndromes, etiology, and prognosis. Neurology 38 (6), 837–848. doi:10.1212/wnl.38.6.837.

Burggraaff, J., Liu, Y., Prieto, J.C., Simoes, J., de Sitter, A., Ruggieri, S., Brouwer, I., Lissenberg-Witte, B.I., Rocca, M.A., Valsasina, P., Ropele, S., Gasperini, C., Gallo, A., Pareto, D., Sastre-Garriga, J., Enzinger, C., Filippi, M., De Stefano, N., Ciccarelli, O., Hulst, H.E.MAGNIMS Study Group, 2021. Manual and automated tissue segmentation confirm the impact of thalamus atrophy on cognition in multiple sclerosis: A multicenter study. NeuroImage. Clinical 29, 102549. doi:10.1016/j.nicl.2020.102549.

Callaghan, MF, Josephs, O, Herbst, M, Zaitsev, M, Todd, N, Weiskopf, N., 2015. An evaluation of prospective motion correction (PMC) for high resolution quantitative MRI. Front Neurosci 9, 97. doi:10.3389/fnins.2015.00097, Published 2015 Mar 25.

Cheek, W.R., Taveras, J.M., 1966. Thalamic tumors. Journal of neurosurgery 24 (2), 505–513. doi:10.3171/jns.1966.24.2.0505.

Deoni, S.C.L., Rutt, B.K., Parrent, A.G., Peters, T.M., 2007. Segmentation of thalamic nuclei using a modified k-means clustering algorithm and high-resolution quantitative magnetic resonance imaging at 1.5 T. NeuroImage 34 (1), 117–126. doi:10.1016/j.neuroimage.2006.09.016.

de Sitter, A., Verhoeven, T., Burggraaff, J., Liu, Y., Simoes, J., Ruggieri, S., Palotai, M., Brouwer, I., Versteeg, A., Wottschel, V., Ropele, S., Rocca, M.A., Gasperini, C., Gallo, A., Yiannakas, M.C., Rovira, A., Enzinger, C., Filippi, M., De Stefano, N., Kappos, L.MAGNIMS Study Group, 2020. Reduced accuracy of MRI deep grey matter segmentation in multiple sclerosis: an evaluation of four automated methods against manual reference segmentations in a multi-center cohort. Journal of neurology 267 (12), 3541–3554. doi:10.1007/s00415-020-10023-1.

Devlin, J.T., Sillery, E.L., Hall, D.A., Hobden, P., Behrens, T.E., Nunes, R.G., Clare, S., Matthews, P.M., Moore, D.R., Johansen-Berg, H., 2006. Reliable identification of the auditory thalamus using multi-modal structural analyses. NeuroImage 30 (4), 1112–1120. doi:10.1016/j.neuroimage.2005.11.025.

Elvsåshagen, T., Shadrin, A., Frei, O., van der Meer, D., Bahrami, S., Kumar, V.J., Smeland, O., Westlye, L.T., Andreassen, O.A., Kaufmann, T., 2021. The genetic architecture of the human thalamus and its overlap with ten common brain disorders. Nature Communications 12 (1), 2909. doi:10.1038/s41467-021-23175-z.

Fujita, N., Tanaka, H., Takanashi, M., Hirabuki, N., Abe, K., Yoshimura, H., Nakamura, H., 2001. Lateral geniculate nucleus: anatomic and functional identification by use of MR imaging. AJNR. American journal of neuroradiology 22 (9), 1719–1726.

Geier, K.T., Buchsbaum, B.R., Parimoo, S., Olsen, R.K., 2020. The role of anterior and medial dorsal thalamus in associative memory encoding and retrieval. Neuropsychologia 148, 107623. doi:10.1016/j.neuropsychologia.2020.107623.

Glasser, M.F., Sotiropoulos, S.N., Wilson, J.A., Coalson, T.S., Fischl, B., Andersson, J.L., Xu, J., Jbabdi, S., Webster, M., Polimeni, J.R., Van Essen, D.C., Jenkinson, M., 2013. The minimal preprocessing pipelines for the Human Connectome Project. NeuroImage 80, 105–124. doi:10.1016/j.neuroimage.2013.04.127.

Glatard, T., Lewis, L.B., Ferreira da Silva, R., Adalat, R., Beck, N., Lepage, C., Rioux, P., Rousseau, M.-E., Sherif, T., Deelman, E., Khalili-Mahani, N., Evans, A.C., 2015. Reproducibility of neuroimaging analyses across operating systems. Frontiers in Neuroinformatics 9. doi:10.3389/fninf.2015.00012.

Gringel, T., Schulz-Schaeffer, W., Elolf, E., Frölich, A., Dechent, P., Helms, G., 2009. Optimized high-resolution mapping of magnetization transfer (MT) at 3 Tesla for direct visualization of substructures of the human thalamus in clinically feasible measurement time. Journal of magnetic resonance imaging: JMRI 29 (6), 1285–1292. doi:10.1002/jmri.21756.

Gronenschild, E.H.B.M., Habets, P., Jacobs, H.I.L., Mengelers, R., Rozendaal, N., Os, J.van, Marcelis, M., 2012. The Effects of FreeSurfer Version, Workstation Type, and Macintosh Operating System Version on Anatomical Volume and Cortical Thickness Measurements. PLOS ONE 7 (6), e38234. doi:10.1371/journal.pone.0038234.

Horien, C., Noble, S., Greene, A.S., Lee, K., Barron, D.S., Gao, S., O'Connor, D., Salehi, M., Dadashkarimi, J., Shen, X., Lake, E.M.R., Constable, R.T., Scheinost, D., 2021. A hitchhiker's guide to working with large, open-source neuroimaging datasets. Nature Human Behaviour 5 (2), 185–193. doi:10.1038/s41562-020-01005-4.

Huang, A.S., Rogers, B.P., Woodward, N.D., 2019. Disrupted modulation of thalamus activation and thalamocortical connectivity during dual task performance in schizophrenia. Schizophrenia Research 210, 270–277. doi:10.1016/j.schres.2018.12.022.

Iglehart, C., Monti, M., Cain, J., Tourdias, T., Saranathan, M., 2020. A systematic comparison of structural-, structural connectivity-, and functional connectivity-based thalamus parcellation techniques. Brain structure & function 225 (5), 1631–1642. doi:10.1007/s00429-020-02085-8.

Iglesias, J.E., Augustinack, J.C., Nguyen, K., Player, C.M., Player, A., Wright, M., Roy, N., Frosch, M.P., McKee, A.C., Wald, L.L., Fischl, B., Van Leemput, K.Alzheimer's Disease Neuroimaging Initiative, 2015. A computational atlas of the hippocampal formation using ex vivo, ultra-high resolution MRI: Application to adaptive segmentation of in vivo MRI. NeuroImage 115, 117–137. doi:10.1016/j.neuroimage.2015.04.042.

Iglesias, J.E., Insausti, R., Lerma-Usabiaga, G., Bocchetta, M., Van Leemput, K., Greve, D.N., van der Kouwe, A., Fischl, B., Caballero-Gaudes, C., Paz-Alonso, P.M., 2018. A probabilistic atlas of the human thalamic nuclei combining ex vivo MRI and histology. NeuroImage 183, 314–326. doi:10.1016/j.neuroimage.2018.08.012.

Iglesias, J.E., Van Leemput, K., Golland, P., Yendiki, A., 2019. Joint inference on structural and diffusion MRI for sequence-adaptive Bayesian segmentation of thalamic nuclei with probabilistic atlases. In: Information Processing in Medical Imaging : Proceedings of the ... Conference, 11492, pp. 767–779. doi:10.1007/978-3-030-20351-1_60.

Johansen-Berg, H., Behrens, T.E.J., Sillery, E., Ciccarelli, O., Thompson, A.J., Smith, S.M., Matthews, P.M., 2005. Functional–Anatomical Validation and Individual Variation of Diffusion Tractography-based Segmentation of the Human Thalamus. Cerebral Cortex 15 (1), 31–39. doi:10.1093/cercor/bhh105.

Jones, E.G., 2012. The Thalamus. Springer Science & Business Media.

Kanowski, M., Voges, J., Tempelmann, C., 2010. Delineation of the nucleus centre median by proton density weighted magnetic resonance imaging at 3 T. Operative neurosurgery (Hagerstown, Md.) 66 (suppl_1). doi:10.1227/01.NEU.0000348560.85056.63.

Keller, S.S., Gerdes, J.S., Mohammadi, S., Kellinghaus, C., Kugel, H., Deppe, K., Ringelstein, E.B., Evers, S., Schwindt, W., Deppe, M., 2012. Volume estimation of the thalamus using freesurfer and stereology: consistency between methods. Neuroinformatics 10 (4), 341–350. doi:10.1007/s12021-012-9147-0.

Kiar, G., Castro, P., de, O., Rioux, P., Petit, E., Brown, S.T., Evans, A.C., Glatard, T., 2020. Comparing perturbation models for evaluating stability of neuroimaging pipelines. The International Journal of High Performance Computing Applications doi:10.1177/1094342020926237.

Kim, D.-J., Park, B., Park, H.-J., 2013. Functional connectivity-based identification of subdivisions of the basal ganglia and thalamus using multilevel independent component analysis of resting state fMRI. Human Brain Mapping 34 (6), 1371–1385. doi:10.1002/hbm.21517.

Krauth, A., Blanc, R., Poveda, A., Jeanmonod, D., Morel, A., Székely, G., 2010. A mean three-dimensional atlas of the human thalamus: Generation from multiple histological data. NeuroImage 49 (3), 2053–2062. doi:10.1016/j.neuroimage.2009.10.042.

Kumar, V.J., van Oort, E., Scheffler, K., Beckmann, C.F., Grodd, W., 2017. Functional anatomy of the human thalamus at rest. NeuroImage 147, 678–691. doi:10.1016/j.neuroimage.2016.12.071.

Lambert, C., Simon, H., Colman, J., Barrick, T.R., 2017. Defining thalamic nuclei and topographic connectivity gradients in vivo. NeuroImage 158, 466–479. doi:10.1016/j.neuroimage.2016.08.028.

Liebermann, D., Ploner, C.J., Kraft, A., Kopp, U.A., Ostendorf, F., 2013. A dysexecutive syndrome of the medial thalamus. Cortex; a journal devoted to the study of the nervous system and behavior 49 (1), 40–49. doi:10.1016/j.cortex.2011.11.005.

Magnotta, V.A., Gold, S., Andreasen, N.C., Ehrhardt, J.C., Yuh, W.T.C., 2000. Visualization of Subthalamic Nuclei with Cortex Attenuated Inversion Recovery MR Imaging. NeuroImage 11 (4), 341–346. doi:10.1006/nimg.2000.0552.

Makowski, C., Béland, S., Kostopoulos, P., Bhagwat, N., Devenyi, G.A., Malla, A.K., Joober, R., Lepage, M., Chakravarty, M.M., 2018. Evaluating accuracy of striatal, pallidal, and thalamic segmentation methods: Comparing automated approaches to manual delineation. NeuroImage 170, 182–198. doi:10.1016/j.neuroimage.2017.02.069.

McNab, J.A., Jbabdi, S., Deoni, S.C., Douaud, G., Behrens, T.E., Miller, K.L., 2009. High resolution diffusion-weighted imaging in fixed human brain using diffusion-weighted steady state free precession. NeuroImage 46 (3), 775–785. doi:10.1016/j.neuroimage.2009.01.008.

Monchi, O., Petrides, M., Petre, V., Worsley, K., Dagher, A., 2001. Wisconsin Card Sorting revisited: distinct neural circuits participating in different stages of the task identified by event-related functional magnetic resonance imaging. The Journal of neuroscience: the official journal of the Society for Neuroscience 21 (19), 7733–7741. doi:10.1523/JNEUROSCI.21-19-07733.2001.

Morel, A., 2007. Stereotactic Atlas of the Human Thalamus and Basal Ganglia. CRC Press.

Morel, A., Magnin, M., Jeanmonod, D., 1997. Multiarchitectonic and stereotactic atlas of the human thalamus. Journal of Comparative Neurology 387 (4), 588–630. doi:10.1002/(SICI)1096-9861(19971103)387:4<588::AID-CNE8>3.0.CO;2-Z.

Najdenovska, E., Alemán-Gómez, Y., Battistella, G., Descoteaux, M., Hagmann, P., Jacquemont, S., Maeder, P., Thiran, J.-P., Fornari, E., Bach Cuadra, M., 2018. In-vivo probabilistic atlas of human thalamic nuclei based on diffusion- weighted magnetic resonance imaging. Scientific Data 5. doi:10.1038/sdata.2018.270.

Ou, Y., Akbari, H., Bilello, M., Da, X., Davatzikos, C., 2014. Comparative Evaluation of Registration Algorithms in Different Brain Databases With Varying Difficulty: Results and Insights. IEEE Transactions on Medical Imaging 33 (10), 2039–2065. doi:10.1109/TMI.2014.2330355.

Pajula, J., Kauppi, J.-P., Tohka, J., 2012. Inter-Subject Correlation in fMRI: Method Validation against Stimulus-Model Based Analysis. PLOS ONE 7 (8), e41196. doi:10.1371/journal.pone.0041196.

Park, J., Park, K.M., Jo, G., Lee, H., Choi, B.S., Shin, K.J., Ha, S., Park, S., Lee, H., Kim, H.Y., 2020. An investigation of thalamic nuclei volumes and the intrinsic thalamic structural network based on motor subtype in drug naïve patients with Parkinson's disease. Parkinsonism & Related Disorders 81, 165–172. doi:10.1016/j.parkreldis.2020.10.044.

Partlow, G.D., del Carpio-O'Donovan, R., Melanson, D., Peters, T.M., 1992. Bilateral thalamic glioma: review of eight cases with personality change and mental deterioration. AJNR. American journal of neuroradiology 13 (4), 1225–1230.

Saranathan, M., Tourdias, T., Bayram, E., Ghanouni, P., Rutt, B.K., 2015. Optimization of white-matter-nulled magnetization prepared rapid gradient echo (MP-RAGE) imaging. Magnetic Resonance in Medicine 73 (5), 1786–1794. doi:10.1002/mrm.25298.

Schepers, I.M., Beck, A.K., Bräuer, S., Schwabe, K., Abdallat, M., Sandmann, P., Dengler, R., Rieger, J.W., Krauss, J.K., 2017. Human centromedian-parafascicular complex signals sensory cues for goal-oriented behavior selection. NeuroImage 152, 390–399. doi:10.1016/j.neuroimage.2017.03.019.

Schmahmann, J.D., 2003. Vascular syndromes of the thalamus. Stroke 34 (9), 2264–2278. doi:10.1161/01.STR.0000087786.38997.9E.

Smith, S.M., Beckmann, C.F., Andersson, J., Auerbach, E.J., Bijsterbosch, J., Douaud, G., Duff, E., Feinberg, D.A., Griffanti, L., Harms, M.P., Kelly, M., Laumann, T., Miller, K.L., Moeller, S., Petersen, S., Power, J., Salimi-Khorshidi, G., Snyder, A.Z., Vu, A.T., Glasser, M.F., 2013. Resting-state fMRI in the Human Connectome Project. NeuroImage 80, 144–168. doi:10.1016/j.neuroimage.2013.05.039.

Sotiropoulos, S.N., Jbabdi, S., Xu, J., Andersson, J.L., Moeller, S., Auerbach, E.J., Glasser, M.F., Hernandez, M., Sapiro, G., Jenkinson, M., Feinberg, D.A., Yacoub, E., Lenglet, C., Van Essen, D.C., Ugurbil, K., Behrens, T.E.J., 2013. Advances in diffusion MRI acquisition and processing in the Human Connectome Project. NeuroImage 80, 125–143. doi:10.1016/j.neuroimage.2013.05.057.

Su, J.H., Thomas, F.T., Kasoff, W.S., Tourdias, T., Choi, E.Y., Rutt, B.K., Saranathan, M., 2019. Thalamus Optimized Multi Atlas Segmentation (THOMAS): Fast, fully automated segmentation of thalamic nuclei from structural MRI. NeuroImage 194, 272–282. doi:10.1016/j.neuroimage.2019.03.021.

Taha, A.A., Hanbury, A., 2015. Metrics for evaluating 3D medical image segmentation: Analysis, selection, and tool. BMC Medical Imaging 15 (1), 29. doi:10.1186/s12880-015-0068-x.

Tourdias, T., Saranathan, M., Levesque, I.R., Su, J., Rutt, B.K., 2014. Visualization of intra-thalamic nuclei with optimized white-matter-nulled MPRAGE at 7T. NeuroImage 84, 534–545. doi:10.1016/j.neuroimage.2013.08.069.

Van der Werf, Y.D., Scheltens, P., Lindeboom, J., Witter, M.P., Uylings, H.B., Jolles, J., 2003. Deficits of memory, executive functioning and attention following infarction in the thalamus; a study of 22 cases with localised lesions. Neuropsychologia 41 (10), 1330–1344. doi:10.1016/s0028-3932(03)00059-9.

Van der Werf, Y.D., Witter, M.P., Uylings, H.B., Jolles, J., 2000. Neuropsychology of infarctions in the thalamus: a review. Neuropsychologia 38 (5), 613–627. doi:10.1016/s0028-3932(99)00104-9.

Van Essen, D.C., Smith, S.M., Barch, D.M., Behrens, T.E., Yacoub, E., Ugurbil, K., Consortium, WU-Minn HCP, 2013. The WU-Minn Human Connectome Project: an overview. NeuroImage 80, 62–79. doi:10.1016/j.neuroimage.2013.05.041.

Whiting, B.B., Whiting, A.C., Whiting, D.M., 2018. Thalamic Deep Brain Stimulation. Current Concepts in Movement Disorder Management 33, 198–206. doi:10.1159/000481104.

Wiegell, M.R., Tuch, D.S., Larsson, H.B.W., Wedeen, V.J., 2003. Automatic segmentation of thalamic nuclei from diffusion tensor magnetic resonance imaging. NeuroImage 19 (2), 391–401. doi:10.1016/S1053-8119(03)00044-2.

Williams, B., Lindner, M., 2020. pyfMRIqc: A Software Package for Raw fMRI Data Quality Assurance. Journal of Open Research Software 8 (1), 23. doi:10.5334/jors.280, http://doi.org/.

Wolff, M., Vann, S.D., 2019. The Cognitive Thalamus as a Gateway to Mental Representations. Journal of Neuroscience 39 (1), 3–14. doi:10.1523/JNEUROSCI.0479-18.2018.

Yang, S., Meng, Y., Li, J., Li, B., Fan, Y.-S., Chen, H., Liao, W., 2020. The thalamic functional gradient and its relationship to structural basis and cognitive relevance. NeuroImage 218, 116960. doi:10.1016/j.neuroimage.2020.116960.

Zaitsev, M., Maclaren, J., Herbst, M., 2015. Motion artifacts in MRI: A complex problem with many partial solutions. Journal of magnetic resonance imaging: JMRI 42 (4), 887–901. doi:10.1002/jmri.24850.

Zhang, D., Snyder, A.Z., Fox, M.D., Sansbury, M.W., Shimony, J.S., Raichle, M.E., 2008. Intrinsic Functional Relations Between Human Cerebral Cortex and Thalamus. Journal of Neurophysiology 100 (4), 1740–1748. doi:10.1152/jn.90463.2008.